EDITORS' CHOICE

Coupling k Convection-Diffusion and Laplace Equations in an Open-Source CFD Model for Tertiary Current Distribution Calculations

A. N. Colli [z] **and J. M. Bisang**

Universidad Nacional del Litoral, CONICET, Programa de Electroquímica Aplicada e Ingeniería Electroquímica (PRELINE), Facultad de Ingeniería Química, S3000AOM Santa Fe, Argentina

A mathematical model to calculate tertiary current distributions in electrochemical reactors is presented taking into account the potential and concentration fields together with the hydrodynamics under laminar or turbulent conditions. Multiple reactions with different kinetic controls are considered at both electrodes. The computational algorithm solving the model was implemented in OpenFOAM. It allows the calculations for a given local potential at the working electrode, potentiostatic control, or for a fixed cell potential difference and also for a current flowing through the cell, galvanostatic operation. The model was validated by using the reduction of ferricyanide and the oxidation of ferrocyanide from dilute solutions as main test reactions and hydrogen and oxygen evolution as secondary ones, in a modified hydrocyclone. A close agreement between experimental and predicted current distributions was obtained. The hydrocyclone presents a promising electrochemical performance being the mass-transfer conditions in its cylindrical part better than in the conical region. The computational tool developed in this paper can be employed to optimize both cells stack design and system operation conditions. Likewise, the algorithm can also be used to check, when limiting current studies are needed, whether the desired reaction is under mass-transfer or charge-transfer control for a given geometric configuration.
 [DOI: 10.1149/2.0132001JES]

Manuscript submitted July 26, 2019; revised manuscript received September 16, 2019. Published October 9, 2019. *This paper is part of the JES Focus Issue on Mathematical Modeling of Electrochemical Systems at Multiple Scales in Honor of Richard Alkire.*

The current distribution strongly affects the performance of electrochemical reactors; this has motivated intense studies of the variables that condition it in order to control or predict its impact. Thus, two extreme situations have arisen to analyze this complex problem.[1–3] A first strategy has been to consider only the electrical potential and the concentration variations in the solution phase are neglected. Hence, it results the primary current distribution when the kinetics are disregarded or the secondary one if only the charge-transfer overvoltages are considered. The second strategy is the opposite of the previous one, given rise to the tertiary current distribution. The development of new computational algorithms has motivated that in recent years methods were proposed to make more efficient the calculation of the current distributions based on the first strategy[4,5] or in accordance with the second approach.[6–8] Although these calculation procedures are very useful because they allow representing reactors in industrial practice, in some cases it becomes necessary to take into account that the electrochemical reaction rates depend on both the electrical potential difference between the electrode and the adjacent solution and the surface concentration of reactant species. The solution of such a problem is also called tertiary current distribution, which was recently reviewed.[9]

Several authors, in order to obtain an answer for a so complex task, proposed models with simplified assumptions. Thus, it was considered a constant hypothetical diffusion layer,[10] a constant mass-transfer coefficient evaluated with the help of the Damkhöler number[11] or a semi-analytical method based on a voltage balance in simple geometries.[12] Other researchers[13–15] assumed that the counter electrode reaction takes place at a constant applied current density, which seems to be a reasonable assumption for electrochemical systems with a nearly uniform primary current distribution. However, for some practical reactors the current distribution at the counter electrode affects the behavior of the working electrode. Likewise, Yang and West[16] assumed constant values for both concentration and potential at the outer boundary away from the electrode. More recently, Rivera et al.[17] considered, for a parallel-plate electrochemical reactor with one reaction at each electrode, the Reynolds-averaged Navier-Stokes equation to take into account the bulk-flow dynamics and a wall function in the proximity of solid surfaces. The treatment of separate regions is attractive but it becomes restricted to flows that result in a thin diffusion layer. Often a more complicated flow field exists; for example, recirculation or boundary-layer separation may occur near cavities or protrusions on surfaces.[18]

Finally, calculations of the tertiary current distributions were also performed for particular cases. Thus, Harb and Alkire[19] simulated the propagation of a pit in a corrosion study taking into account the migration of the species. Chung[18] focused the attention in an unsteady laminar natural convection multi-ion electrodeposition system. Byrne et al.[20] reported a numerical model that calculates the current density distribution and concentration profiles in order to elucidate the chlorate process, and recently Weber et al.[21] presented a model for computing three-dimensional current and potential distributions, which accounts for internal voltage jumps applied to liquid metal batteries.

Despite the important contributions of the above papers, the simultaneous calculation of the concentration and potential profiles with different boundary conditions is required in some electrochemical reactors with a more complex geometry.[22–24] Thus, this paper aims to produce a mathematical tool in order to simulate the tertiary current distribution taking into account simultaneously k averaged convection-diffusion equations and Laplace's equation for the potential field. A multi-reaction scheme is considered at the working electrode and realistic kinetics are assumed at the counter electrode. The simulations are validated by comparison with experimental results obtained with a modified hydrocyclone.

Mathematical Modeling

Governing equations.—The design of an electrochemical reactor demands the evaluation of the local current density, j, at the surface of each electrode. The i^{th} reaction rate is given by

$$j_i = \text{Function}(\phi_s^w, \phi^w, E_0^i, c_k^w) \quad [1]$$

here c_k is the concentration of the k^{th} species, E_0^i is the reversible electrode potential of the i^{th} reaction, ϕ_s and ϕ are the potentials at the solid and fluid phases, respectively, and the superscript w denotes that the variable is evaluated at the electrode surface. Assuming that the electrochemical reactions are not coupled is

$$j = \sum_i j_i \quad [2]$$

According to Eq. 1 the evaluation of the current density involves knowing the concentrations and the potential of both phases at each

[z]E-mail: ancolli@gmail.com

point of the electrode surface. Thus, the calculation of the concentration requires the simultaneous solution of the transient time-averaged convection-diffusion equation

$$\frac{\partial c_k}{\partial t} + \boldsymbol{u} \cdot \nabla c_k = \nabla \cdot [(D_k + D_T)\nabla c_k] \quad [3]$$

with the incompressible continuity equation

$$\nabla \cdot \boldsymbol{u} = 0 \quad [4]$$

and the Navier-Stokes equations for an incompressible and Newtonian fluid without external forces

$$\frac{\partial \boldsymbol{u}}{\partial t} + \boldsymbol{u} \cdot \nabla \boldsymbol{u} = -\nabla p + \nabla \cdot \left\{(\nu + \nu_T)\left[\nabla \boldsymbol{u} + (\nabla \boldsymbol{u})^T\right]\right\} \quad [5]$$

where D_T and ν_T are the turbulent diffusion coefficient and the turbulent viscosity, respectively, $\boldsymbol{u}$ and p represent the local values of flow velocity and density normalized pressure under laminar flow calculations or their time-averaged values when the turbulent regime is considered. In this last case, Eqs. 4 and 5 are known as Reynolds-averaged Navier–Stokes (RANS) approach. In Eq. 3 the migration term was disregarded because practical electrochemical reactors use a supporting electrolyte in order to improve the fluid phase conductivity, κ. Likewise, the solid phase can be considered as an isopotential due to its higher conductivity in comparison with that of the fluid phase, which potential may be approached by the Laplace equation

$$\nabla \cdot (\kappa \nabla \phi) = 0 \quad [6]$$

Eq. 6 represents a convenient assumption in order to simplify the mathematical treatment becoming less cumbersome the numerical calculations.

The turbulent viscosity can be obtained by solving additional equations from one of the almost twenty turbulence models currently existing in OpenFOAM,[25] while a constant value of the turbulent Schmidt number, Sc_T, defined as

$$Sc_T = \frac{\nu_T}{D_T} \quad [7]$$

can be used for the evaluation of the turbulent diffusion coefficient. In the present contribution the turbulence conditions were considered according to the SST k-ω model with curvature correction[26] in steady-state conditions. Likewise, it was assumed $Sc_T = 0.2$ which was previously obtained by a sensitive study for the same electrochemical reaction under similar hydrodynamic conditions.[26] Therefore, the complete set of Eqs. 1–7, together with any turbulence model existing in OpenFOAM is proposed here as a strategy to calculate the tertiary current distribution.

Boundary conditions, BC.—The k^{th} concentration at each electrode surface is given by

$$-\frac{\nu_e F D_k}{\nu_k}\left.\frac{\partial c_k}{\partial n}\right|_w = j_i \quad [8]$$

Being n the coordinate normal to the boundary in direction of the interior of the fluid phase, ν_e and ν_k the stoichiometric coefficients for the electron and for the k^{th} species, involved in the i^{th} reaction, respectively, ν_k is positive for reduced species and negative for oxidized ones. Eq. 8 shows that the diffusion flow equalizes the kinetic expression.

For the potential of the fluid phase it is assumed the validity of the Ohm's law and taking into account Eq. 2 results in

$$-\kappa \left.\frac{\partial \phi}{\partial n}\right|_w = \sum_i j_i \quad [9]$$

Finally, the usual boundary conditions for the hydrodynamics were used,[8,26] which are summarized in Table I.

Numerical discretization and linearization of non-linear terms.—Applying a Taylor series expansion to the right hand sides of Eqs. 8 and 9, and neglecting high order terms yields

$$\frac{\nu_e F D_k}{\nu_k \Delta}\left(c_k^{face} - c_k^{center}\right) = \left[j_i - c\frac{dj_i}{dc}\right]_{c_k^{face,0}} + \left.\frac{dj_i}{dc}\right|_{c_k^{face,0}} c_k^{face} \quad [10]$$

$$\frac{\kappa}{\Delta}\left(\phi^{face} - \phi^{center}\right) = \sum_i \left[j_i - \phi\frac{dj_i}{d\phi}\right]_{\phi^{face,0}} + \sum_i \left.\frac{dj_i}{d\phi}\right|_{\phi^{face,0}} \phi^{face}, \quad [11]$$

respectively, being Δ the distance between the cell center to the interface. Eqs. 10 and 11 are applied at both electrodes. Here, c_k^{center} and ϕ^{center} represent the concentration and the potential in the center of the volume element located immediately near the interface of each electrode, $c_k^{face,0}$ and $\phi^{face,0}$ are the concentration and the potential at the interface extracted from the available data at the previous iteration step, denoted with the superscript 0. Isolating c_k^{face} and ϕ^{face} from Eq. 10 and Eq. 11 is

$$c_k^{face} = \frac{b_k}{1 + a_k} + \frac{1}{1 + a_k} c_k^{center} \quad [12]$$

and

$$\phi^{face} = \frac{B}{1 + A} + \frac{1}{1 + A}\phi^{center} \quad [13]$$

where

$$a_k = -\frac{\nu_k \Delta}{\nu_e F D_k}\left.\frac{dj_i}{dc_k}\right|_{c_k^{face,0}} \quad [14]$$

and

$$b_k = \frac{\nu_k \Delta}{\nu_e F D_k}\left(j_i - c_k\frac{dj_i}{dc_k}\right)_{c_k^{face,0}} \quad [15]$$

Analogously

$$A = -\frac{\Delta}{\kappa}\sum_i \left.\frac{dj_i}{d\phi}\right|_{\phi^{face,0}} \quad [16]$$

and

$$B = \frac{\Delta}{\kappa}\sum_i \left[j_i - \phi\frac{dj_i}{d\phi}\right]_{\phi^{face,0}} \quad [17]$$

Table I. Boundary conditions.

Field	Inlet	Outlet	Walls	Electrodes	Initial Internal
u	$\boldsymbol{u}_{in}$	zeroGradient	noSlip	noSlip	(0,0,0)
$\boldsymbol{p}$	zeroGradient	0	zeroGradient	zeroGradient	0
$\boldsymbol{k}$	*$3/2(TI\,\boldsymbol{u}_{in})^2$	zeroGradient	0	0	Inlet
$\boldsymbol{\omega}$	Internal field	zeroGradient	omegaWallFunction	omegaWallFunction	$10\boldsymbol{u}_{in}/d_h$

*TI is the turbulence intensity, varied between 5 and 20%.

Implementation in OpenFOAM.—A Robin BC can be seen as a weighted combination of Dirichlet BC and Neumann BC. OpenFOAM has a boundary condition called mixed, which is mainly used for switching between the fixed value and the fixed gradient situations on a particular boundary and it is given for each variable, var, by the following expression

$$\mathrm{var}^{\mathrm{face}} = f_{\mathrm{var}}\,\mathrm{VR}_{\mathrm{var}} + (1 - f_{\mathrm{var}})\left(\mathrm{var}^{\mathrm{center}} + \mathrm{VGR}_{\mathrm{var}}\,\Delta\right) \quad [18]$$

here var is ϕ or c_{k}, f is the fractionExpression defined by the user. When $f = 1$, Eq. 18 gives a Dirichlet boundary condition and for $f = 0$ it yields a Neumann one. The Robin case is represented by $0 < f < 1$, being f calculated as explained below. By comparing Eqs. 12 and 18 it is obtained for each electrode and k$^{\mathrm{th}}$ species

$$\mathrm{VGR}_{c_{\mathrm{k}}}\left(\text{reactants, products}\right) = \left[0,\ \frac{\nu_{\neq \mathrm{k}} D_{\mathrm{k}}}{\nu_{\mathrm{k}} D_{\neq \mathrm{k}}}\left.\frac{\partial c_{\mathrm{k}}}{\partial n}\right|_{\mathrm{w}}\right] \quad [19]$$

$$f_{c_{\mathrm{k}}}\left(\text{reactants, products}\right) = \left[\mathrm{a_k}\big/(1 + \mathrm{a_k}),\ 0\right] \quad [20]$$

$$\mathrm{VR}_{c_{\mathrm{k}}}\left(\text{reactants, products}\right) = \left[\mathrm{b_k}\big/\mathrm{a_k},\ 0\right] \quad [21]$$

The subscript $\neq$k denotes the product of the reaction which reactant is k. The set of Eqs. 19 to 21 means that for the reactant species is taken a Robin boundary condition and a Neumann one for the reaction product, characterized by the flux of the species away from the electrode surface. Relating Eq. 13 with Eq. 18 it is obtained for each electrode

$$\mathrm{VGR}_{\phi} = 0 \quad [22]$$

$$f_{\phi} = \mathrm{A}\big/(1 + \mathrm{A}) \quad [23]$$

$$\mathrm{VR}_{\phi} = \mathrm{B}\big/\mathrm{A} \quad [24]$$

For the present simulations and further comparisons with experimental results, it will be considered two electrochemical reactions at each electrode, i.e. one under a combined diffusion and charge-transfer control and the other with this last kinetic control. This reaction scheme is represented by a redox couple as the main reaction and the half-reactions of water splitting as the secondary ones. Then, the proposed model can account for a reversible electrochemical reaction at each electrode and one irreversible reaction without the influence of concentration variations, hydrogen or oxygen evolution. Thus, according to the above statement Eq. 1 at each electrode can be expressed by

$$j_{\mathrm{i}} = \sum_{\mathrm{k=Red-Ox}} j_0^{\mathrm{i}} \frac{c_{\mathrm{k}}^{\mathrm{face}}}{c_{\mathrm{k}}^{\mathrm{b}}} \exp\left(\frac{\phi_{\mathrm{s}} - \phi^{\mathrm{face}} - E_0^{\mathrm{i}}}{b_{\mathrm{T}}^{\mathrm{k}}}\right) = \left(j_{\mathrm{i}}^{\mathrm{k=Red}} + j_{\mathrm{i}}^{\mathrm{k=Ox}}\right) \quad [25]$$

Here $c_{\mathrm{k}}^{\mathrm{b}}$ is the bulk concentration, b_{T} is the Tafel slope, $RT/\alpha F$ or $-RT/(1-\alpha)F$, and j_0 the exchange current density. In the computational calculations, both parameters will be considered positive for anodic reactions and negative for the cathodic case in order to retain the usual sign convention for current density. For the secondary reactions of hydrogen and oxygen evolution is $c_{\mathrm{k}}^{\mathrm{face}} = c_{\mathrm{k}}^{\mathrm{b}}$ giving the Butler-Volmer equation.

Combining Eq. 14 with the first derivative with respect to the concentration of Eq. 25 yields

$$\mathrm{a_k} = -\frac{\nu_{\mathrm{k}}\Delta}{\nu_{\mathrm{e}} F D_{\mathrm{k}}} \frac{j_{\mathrm{i}}^{\mathrm{k}}}{c_{\mathrm{k}}^{\mathrm{face}}} \quad [26]$$

Combining Eq. 15 with Eq. 25 and its first derivative with respect to the concentration results in

$$\mathrm{b_k} = \frac{\nu_{\mathrm{k}}\Delta}{\nu_{\mathrm{e}} F D_{\mathrm{k}}} j_{\mathrm{i}}^{\neq \mathrm{k}} \quad [27]$$

Combining Eq. 16 with the first derivative with respect to the potential of Eq. 25 is

$$\mathrm{A} = \frac{\Delta}{\kappa} \sum_{\mathrm{i}} \left[\sum_{\mathrm{k}} \frac{j_{\mathrm{i}}^{\mathrm{k}}}{b_{\mathrm{T}}^{\mathrm{k}}}\right]_{\phi^{\mathrm{face},0}} \quad [28]$$

Combining Eq. 17 with the first derivative with respect to the potential of Eq. 25 yields

$$\mathrm{B} = \frac{\Delta}{\kappa} \sum_{\mathrm{i}} \left\{\sum_{\mathrm{k}} \left(1 + \frac{\phi^{\mathrm{face}}}{b_{\mathrm{T}}^{\mathrm{k}}}\right) j_{\mathrm{i}}^{\mathrm{k}}\right\}_{\phi^{\mathrm{face},0}} \quad [29]$$

Then, the set of general Equations 18 to 24, valid for any number of reactions and kinetic controls, is combined with Eqs. 26 to 29 for our particular kinetic case. However, the mathematical model is valid for any geometrical configuration of electrochemical reactor.

Potentiostatic and galvanostatic control.—Under a fixed cell potential the electrodes have a known potential difference and it is imposed $\phi_{\mathrm{s}} = 0$ for the solid phase of the cathode and $\phi_{\mathrm{s}} = U$ for that of the anode. A special case is the controlled potential in a given position at the working electrode, called potentiostatic control. Here, giving the desired reference potential, $\phi^{\mathrm{ref\_d}}$, and the actual value for each iteration, ϕ^{ref}, it is possible to update the cell potential difference after each iteration by the following formulae

$$U^{*} = U^{0} + \mathrm{diffRef} \quad [30]$$

where

$$\mathrm{diffRef} = \begin{cases} 0 & \text{if} \quad \left|1 - \phi^{\mathrm{ref\_d}}\big/\phi^{\mathrm{ref}}\right| < \mathrm{Tol} \\ \min\left[\left(\phi^{\mathrm{ref}} - \phi^{\mathrm{ref\_d}}\right), \mathrm{maxRef}\right] & \text{if} \quad \phi^{\mathrm{ref}} > \phi^{\mathrm{ref\_d}} \\ \max\left[\left(\phi^{\mathrm{ref}} - \phi^{\mathrm{ref\_d}}\right), -\mathrm{maxRef}\right] & \text{if} \quad \phi^{\mathrm{ref}} < \phi^{\mathrm{ref\_d}} \end{cases} \quad [31]$$

here maxRef is an input supplied by the user, being 0.1 V the recommended value to prevent overshooting.

On the other hand, when the electrochemical reactor is operated at a fixed known current, the system is in galvanostatic mode and the potential difference between the anode, floating at an unknown potential, and the cathode connected to the ground is obtained by performing an integration of the current density over the anode surface, using Eq. 30 with

$$\mathrm{diffRef} = \begin{cases} 0 & \text{if} \quad \left|\int_{A_{\mathrm{a}}} j_{\mathrm{a}} dA \big/ I - 1\right| < \mathrm{Tol} \\ -b_{\mathrm{T}}^{\mathrm{Red}}\left(\int_{A_{\mathrm{a}}} j_{\mathrm{a}} dA \big/ I - 1\right) & \text{if} \quad \left|\int_{A_{\mathrm{a}}} j_{\mathrm{a}} dA \big/ I - 1\right| > \mathrm{Tol} \end{cases} \quad [32]$$

It must pointed out that the constrain presented in Eq. 32 comes from a Newton-Raphson analysis as was discussed previously.[4]

Finally, in order to explicitly under- or over-relax (more stability or faster convergence) the numerical scheme and to prevent unphysical results, the following equation is applied

$$U = U^{0} + \beta\left\{\max\left[\min\left(U^{*}, \max U\right), \phi^{\mathrm{ref\_d}}\right] - U^{0}\right\} \quad [33]$$

where β is the under-over relaxation parameter (recommended values are 0.3 for potentiostatic control and up to 1.3 for galvanostatic control) and max$U$ is the maximum cell potential difference expected for the simulation. The proposed algorithm is shown schematically in Fig. 1 and its implementation can be found in a GitHub link.[27] Thus, a solver, new boundary conditions implemented as codedMixed, post-processing utilities and a concise example on how to use the validated tool are provided in the mentioned link.

Benefits and limitations of the proposed approach.—The following features can be recognized:

a) The source code is accessible and modifiable. It allows adding more involved species and modifying the kinetic expressions.
b) There are no licence costs. User can use, share and modify it for free.
c) There is a wide range of turbulent models and post-processing utilities, already existing in OpenFOAM, ready to be used in the present strategy.
d) Modifications in the program to take into account the gas phase or migration of charged species can be implemented.

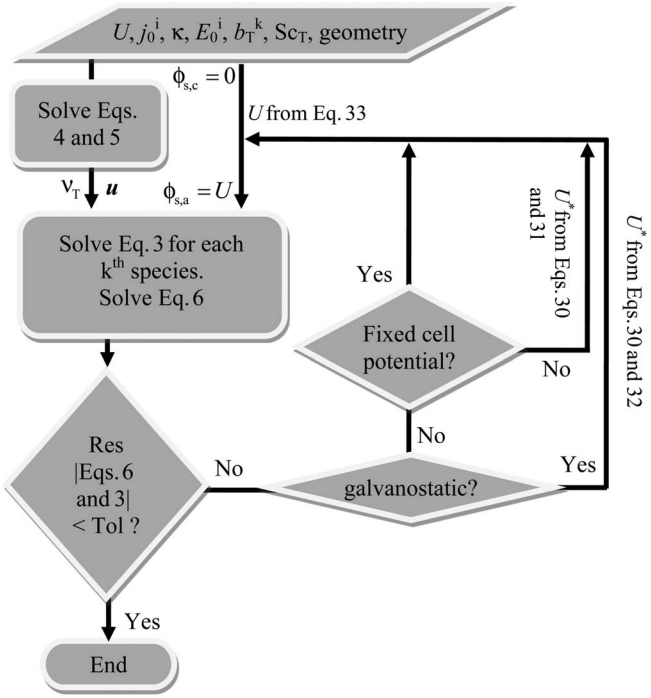

Figure 1. Flow chart for solving the current-potential distribution problem for a monopolar electrochemical cell under fixed cell potential difference, potentiostatic or galvanostatic control.

e) As limitation it can be stated that this computational strategy is more technical and it may be harder to use in comparison to commercial software, demanding trained people for its modification.

Computational characteristics.—The computational algorithm based on the above mathematical model was checked by comparison with experimental results obtained with a modified hydrocyclone as electrochemical reactor. Table II reports on the solution and algorithm control imposed for the computation of each field. Convergence was monitored by following the residuals and the total current. The final mesh was obtained after a grid-independence study[5,26] comparing the ratios of the total current for 3 meshes for the highest values of both flow rate and controlled potential. Thus, the finest grid consisted in a structured mesh 320 per 80 cells in θ-*r* directions, and 25 cells per segment (plus 5 cells for each polyamide ring) in the *y* direction, giving nearly 10 million cells for the whole reactor. A non-uniform mesh grading was used for the grid size in the *r* and *y* directions, which was gradually varied according to different geometric progressions that allows having grid points inside the viscous sublayer and inside the boundary layer of each species (first computational points were located at 5×10^{-7} m from the wall).

With regard to the discretization, it was used limited schemes for the gradients and laplacians, bounded Gauss upwind for the divergence in the case of velocity, while bounded Gauss limitedLinear 1 for the rest of variables.

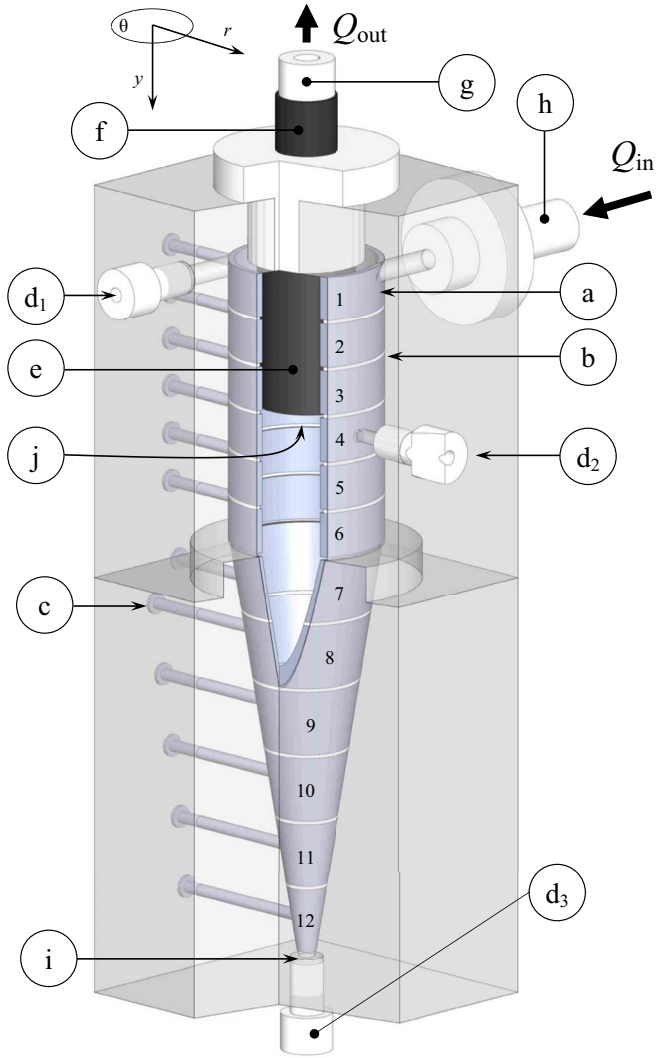

Figure 2. Schematic representation of the modified electrochemical hydrocyclone reactor with a segmented cathode. (a) Segmented cathode; (b) insulating rings; (c) electrical connection to segmented cathode; (d_2) connection of Haber-Luggin capillary for cathodic potential control; (d_1) and (d_3) ports for cathodic potential measurement; (e) anode; (f) electrical connection to anode; (g) electrolyte outlet; (h) electrolyte inlet; (i) spigot; (j) vortex finder. The numbers indicate the position of the segments and the arrows the flow of the electrolyte. Q_{in} and Q_{out}: inlet or outlet volumetric flow rate.

Experimental

An exploded view of the reactor is displayed in Fig. 2. The cylindrical part of the reactor was made of six 316 stainless steel segments,

Table II. Solution and algorithm control.

Field	Tolerance for the linear system of eqs.	Relative tolerance (Maximum iterations)	Relaxationfactors	Tolerance for the residual control	Solver (Smoother)
u	1×10^{-7}	0 (–)	0.9	1×10^{-6}	smoothSolver (symGaussSeidel)
p	1×10^{-6}	0 (–)	0.7	1×10^{-5}	GAMG (GaussSeidel)
k	1×10^{-8}	0 (–)	0.9	1×10^{-6}	smoothSolver (symGaussSeidel)
ω	1×10^{-10}	0 (–)	0.9	1×10^{-6}	smoothSolver (symGaussSeidel)
$c_{\text{Red-Ox}}$	1×10^{-7}	1×10^{-4} (100)	0.95	1×10^{-5}	PBiCG (DILU)
ϕ	1×10^{-7}	0.1 (100)	–	1×10^{-6}	PCG (DIC)

Table III. Physicochemical properties of the ferricyanide/ferrocyanide (Red/Ox) solution.

Composition	$[K_3Fe(CN)_6] = 11$ (mol/m^3) $[K_4Fe(CN)_6] = 50$ (mol/m^3) $[K_2CO_3] = 650$ (mol/m^3)
κ (S/m)	12.9
pH	13.4
ν (m^2/s)	1.3×10^{-6}
D_{Ox} (m^2/s)	8.1×10^{-10}
D_{Red} (m^2/s)	7.2×10^{-10}

40 mm internal diameter and 12 mm length, being one another insulated by a polyamide ring 1 mm thick; resulting a cylindrical body of 78 mm total length. The conical sector was assembled with six segments, 18 mm length, also insulated by a polyamide ring, 1 mm thick. The total length of the segmented conical part was 113 mm with an angle of 18°. The surface of the cathodic segments was polished with emery paper 2500 grid. The anode was made of a nickel cylinder, 26 mm external diameter and 40 mm length. The tangential inlet port and the vortex finder were both 7 mm in diameter, being the last one concentric with the anode. The dimensions of the hydrocyclone correspond to those of a standardized device.[28] The experiments were carried out potenciostatically controlling the cathodic potential against a saturated calomel electrode, SCE, connected to a Haber-Luggin capillary placed in the cylindrical body at 45 mm from the top. This cathodic potential is called here as controlled potential. Likewise, in order to obtain information about the potential distribution along the electrode length the cathodic potential was also measured in two additional points, i.e. the first near the fluid inlet, at 6 mm from the top, and the second one at the spigot; which are denoted in the following as measured potentials. These connections in order to determine the potential distribution along the axial direction are the main difference with the reactor previously reported;[24] where further experimental details are given. The reactor was made part of a flow circuit system consisting of a pump, a flowmeter and connections to maintain the temperature at the preset value, 30°C.

The back side of each segment and the cathodic current feeder were joined by a calibrated resistor, 0.025 Ω resistance, and the axial current distribution was obtained by measuring the ohmic drop in each of them.

The test reactions were, at the cathode, the electrochemical reduction of ferricyanide and hydrogen evolution as a secondary one. Oxidation of ferrocyanide and oxygen evolution took place as main and side anodic reactions, respectively. The solution was $[K_3Fe(CN)_6] \cong 11$ mol/m^3, $[K_4Fe(CN)_6] \cong 50$ mol/m^3 in 650 mol/m^3 of K_2CO_3 as supporting electrolyte. Table III summarizes the composition and physicochemical properties of the solution, which were measured in the laboratory.

Nitrogen was bubbled in the reservoir for 1 h prior to the experiment in order to remove the dissolved oxygen. A concentration of ferrocyanide five times higher than ferricyanide concentration was chosen in order to compensate that the anodic surface area is 4.15 times smaller than the cathodic one. Thus, the secondary reaction at the counter electrode is decreased maintaining stable concentrations for both species of the redox couple during the experiment. The high concentration of supporting electrolyte was adopted to diminish the oxygen solubility in the electrolyte.[29] Thus, the reduction of the residual oxygen after bubbling nitrogen can be neglected as side cathodic reaction in comparison with the ferricyanide reduction from this dilute solution. Samples of the electrolyte were taken from the reservoir after each experiment and the ferricyanide concentration was spectrophotometrically determined at a wavelength of 422 nm, using a Perkin-Elmer model Lambda 20 double-beam UV-Vis Spectrophotometer with 10 mm glass absorption cells and the supporting electrolyte was used as blank.

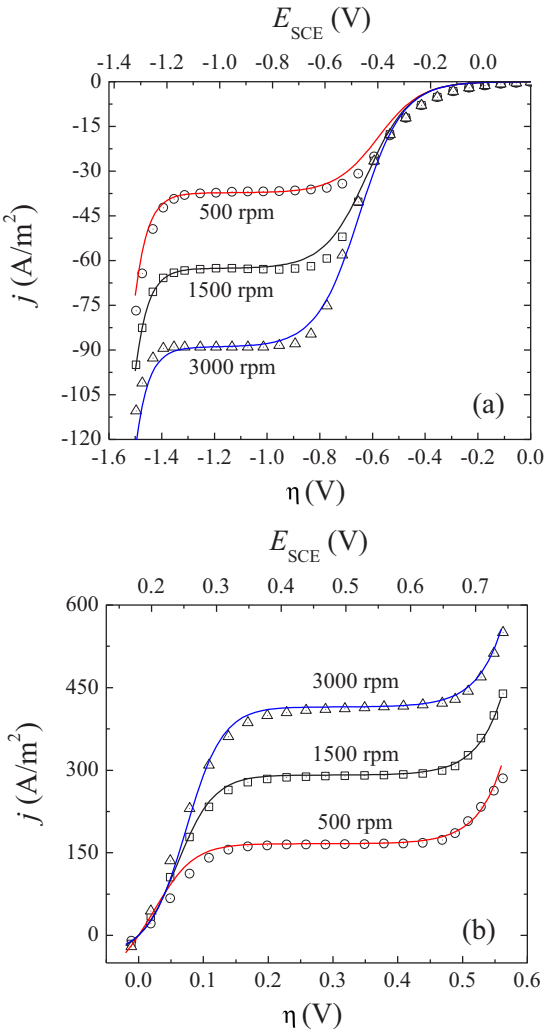

Figure 3. (a) Polarization curves for the ferricyanide reduction at a rotating disk electrode of stainless steel 316. (b) Polarization curves for the ferrocyanide oxidation at a rotating disk electrode of nickel. $[K_3Fe(CN)_6] = 11$ mol/m^3, $[K_4Fe(CN)_6] = 50$ mol/m^3, using 650 mol/m^3 of K_2CO_3 as supporting electrolyte. $T = 30$°C. Potential sweep rate: 1 mV/s. E_0 vs. SCE = 0.180 V.

Kinetic behavior.—Prior to the potential and current distribution measurements, the electrochemical behavior of the anodic and cathodic test reactions were studied at rotating disk electrodes, 3 mm diameter. Fig. 3, Part (a) shows a set of cathodic polarization curves using 316 stainless steel while the anodic ones are reported on Fig. 3 Part (b) using a nickel electrode. The diffusion coefficients declared in Table III were calculated from the limiting current densities reported on Fig. 3 by using the Levich equation. The charge-transfer kinetics parameters, j_0 and α, were obtained by fitting the experimental values to Eq. 34 using a non-linear regression. In the case of the reduction of ferricyanide at 316 stainless steel the experimental data in the potential range outside hydrogen evolution were considered assuming $j_{lim,a} \rightarrow \infty$. For ferrocyanide oxidation at nickel it was used the experimental results where oxygen evolution is not possible and $j_{lim,c}$ was taken from Fig. 3 Part (a). The charge transfer parameters reported on Table IV represent mean values from the correlation of the polarization curves at different rotation speeds.

$$j = \frac{\exp\left(\frac{\alpha F}{RT}\eta\right) - \exp\left(-\frac{(1-\alpha)F}{RT}\eta\right)}{\frac{1}{j_0} + \frac{\exp\left(\frac{\alpha F}{RT}\eta\right)}{j_{lim,a}} - \frac{\exp\left(-\frac{(1-\alpha)F}{RT}\eta\right)}{j_{lim,c}}} \qquad [34]$$

Table IV. Kinetic properties of the ferricyanide/ferrocyanide (Red/Ox) couple and the H_2/O_2 evolution.

$j_{0,\text{Red}-\text{Ox}}$ (stainless steel) (A/m^2)	3.1×10^{-2}
$j_{0,\text{Red}-\text{Ox}}$ (nickel) (A/m^2)	22
$\alpha_{\text{Red}-\text{Ox}}$ (stainless steel)	0.68
$\alpha_{\text{Red}-\text{Ox}}$ (nickel)	0.94
j_{0,H_2} (stainless steel) (A/m^2)	1.1×10^{-1}
j_{0,O_2} (nickel) (A/m^2)	6.85×10^{-5}
α_{H_2} (stainless steel)	0.44
α_{O_2} (nickel)	0.69
E_{0,H_2} (V)	–1.213*
E_{0,O_2} (V)	0.015*

*Referred to the rest potential of the redox couple = 0.18 V vs. SCE.

The overvoltage, η, of the redox couple was referred to the experimental value of the rest potential measured in the deoxygenated electrolyte, 0.180 V against SCE, which coincides with the equilibrium potential calculated from the Nernst equation using an apparent standard potential in alkaline solution of 0.2185 V against SCE.[30] Finally, the charge-transfer kinetic parameters for the secondary reactions were obtained adjusting the partial current densities for hydrogen and oxygen evolution from Fig. 3 to the Butler-Volmer equation, obtained assuming $j_{\text{lim,a}}$ and $j_{\text{lim,c}} \to \infty$ in Eq. 34. The reversible electrode potentials, E_0, for each secondary reaction were corrected for temperature and pH of solution and are reported on Table IV referred to the rest potential of the redox couple.

Results and Discussion

Fig. 4 shows contour plots of the axial, angular and radial velocity profiles for the modified hydrocyclone, obtained by the simpleFoam routine, revealing that the angular velocity is dominant in comparison with the other two components of the velocity. In the axial velocity plot the blue regions denote a downward flow and those with red color an upstream current. The angular velocity rotates in clockwise sense and positive radial velocity profiles are directed from the center to the periphery. The axial and angular profiles in Fig. 4 confirm that the flow in a hydrocyclone is composed by two spirals, rotating in the same sense with opposite direction in the vertical component of velocity.[31] Likewise, comparing the plot on the left-hand side with that on the right-hand side it is observed that, in the conical part, the maximum in the axial velocity profiles coincides with a region where the radial velocity changes its direction to the opposite sense. However, this last behavior in the cylindrical part is altered because a portion of the external downward spiral is bypassed toward the vortex finder of the equipment. Nevertheless, dead zones are not detected. The above discussion demonstrates that the hydrodynamic conditions in the modified hydrocyclone are similar to that of conventional equipments.[32–34]

Fig. 5 Part (a) displays a contour plot of the potential distribution in the fluid phase and Part (b) reports on an exploded view of the cylindrical region near the counter electrode. In Fig. 5 the potential of the cathodic solid phase was considered zero and the controlled potential 1.1 V. Isopotential lines, spaced by 0.064 V in Part (a) and by 0.0256 V in Part (b), are also reported on both graphs showing a more marked potential distribution in axial direction than in the radial coordinate.

Fig. 6 compares typical curves of the experimental and theoretical current distribution for different volumetric flow rates, where a close

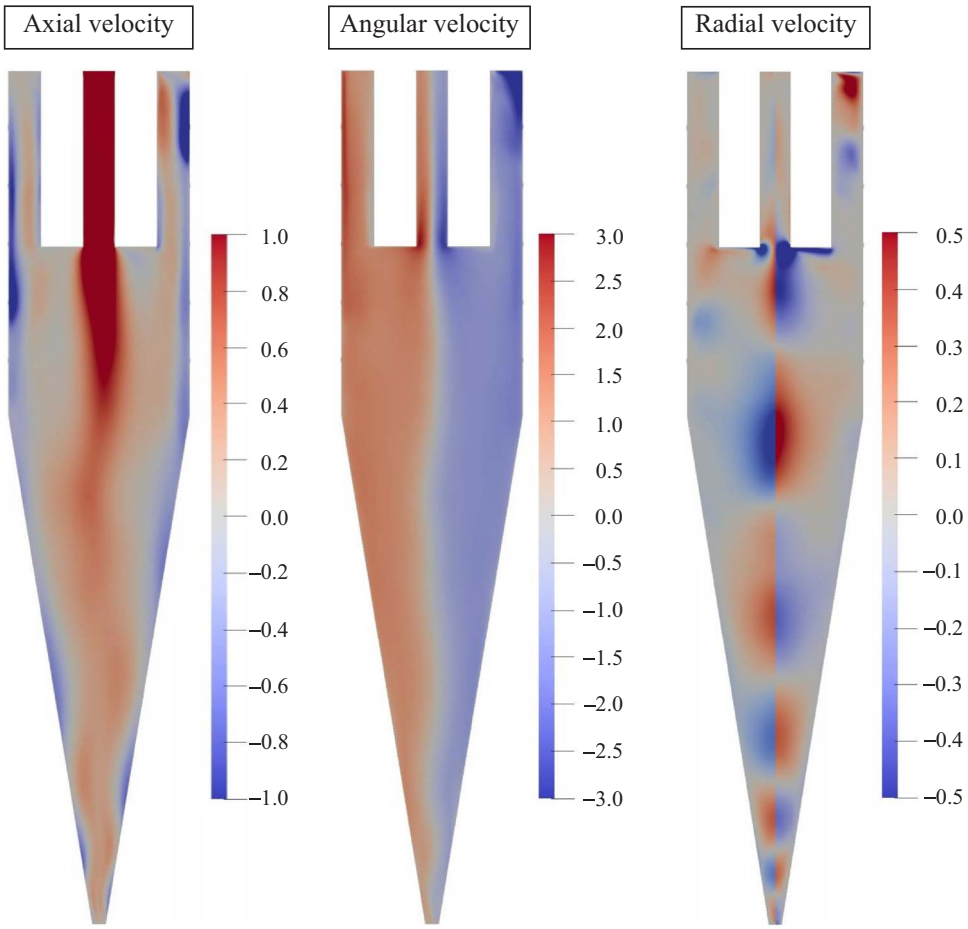

Figure 4. Contour plots for the axial, angular and radial velocity profiles in m/s. $Q = 8.7$ dm^3/min.

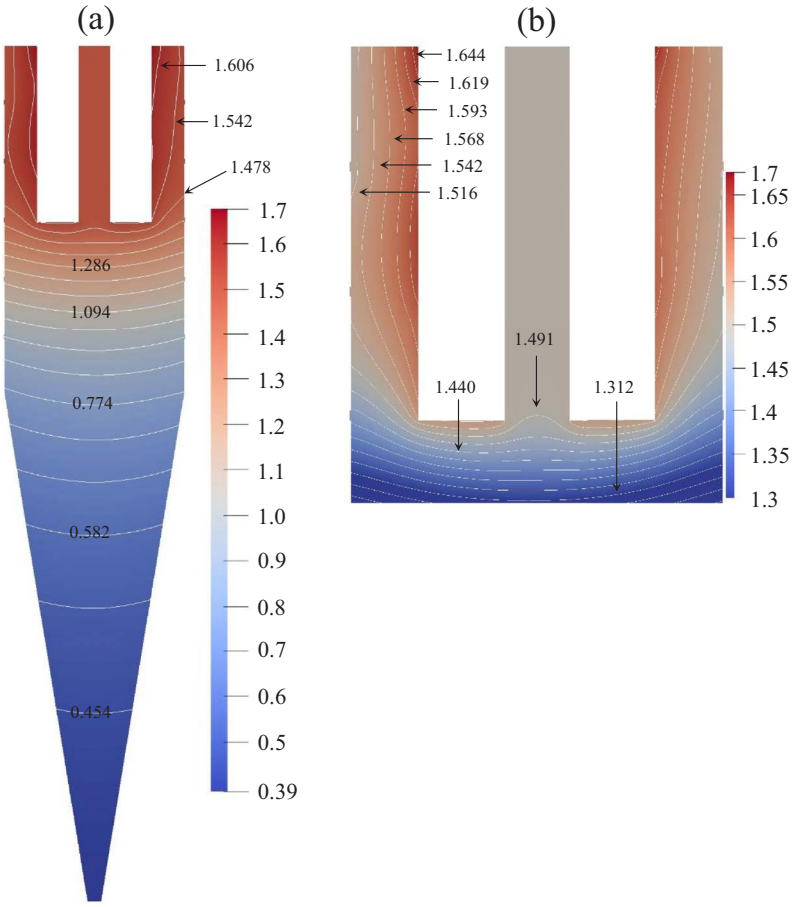

Figure 5. Contour plot for the fluid phase potential distribution in V. $Q = 8.7$ dm^3/min. $E_{SCE} = -1.1$ V.

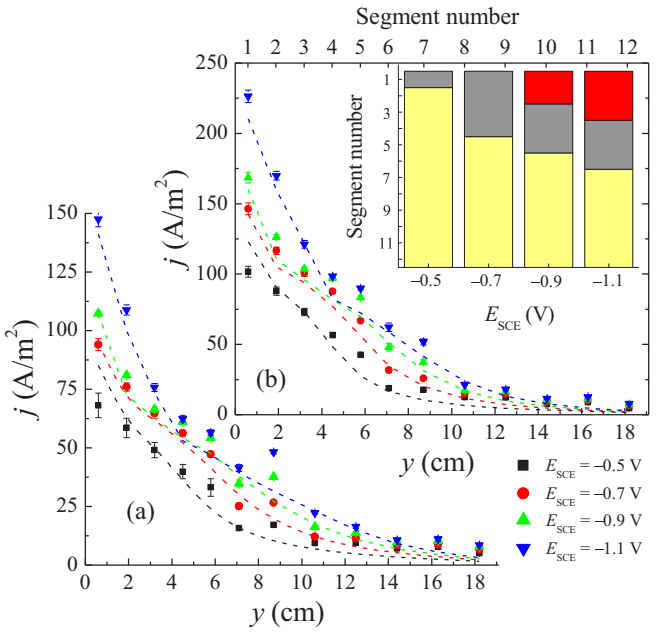

Figure 6. Local current density as a function of the axial position for different values of the applied potential at the cathode. Part (a): $Q = 5.2$ dm^3/min. Part (b): $Q = 8.7$ dm^3/min. Symbols: experimental points. Error bars: 95% confidence interval. Dashed lines: simulations results. Inset: characterization of the limiting current condition for the segments at different potentials. Gray region: under limiting current conditions; light yellow region: below the limiting current; red region: with hydrogen evolution as a secondary reaction.

agreement between both data sets is observed. The experiments were done at four values of the cathodic potentials, i.e. −0.5 V, −0.7 V, −0.9 V and −1.1 V against saturated calomel electrode. According to Fig. 3, at the above first value of the controlled potential the reaction is under sub-limiting current condition, for the two intermediate potentials the main reaction takes place at limiting current and for −1.1 V begins hydrogen evolution as secondary electrochemical reaction. The inset in Fig. 6 displays the current conditions of the segments at different cathodic potentials showing that a limiting current (gray) is achieved at low potentials only in the first segments with the remaining ones being below the limiting current (light yellow). When the potential becomes more negative the mass-transfer control also takes place in the middle segments but in this case hydrogen evolution occurs in the first ones (red). This fact evidences the difficulty to carry out a suitable mass-transfer study, requiring experiments at different potentials in order to identify a potential range at each segment where a limiting current is achieved.

Fig. 7 reports on the cathodic potentials at the top, E_{SCE}^{upper}, and at the spigot, E_{SCE}^{lower}, of the hydrocyclone as a function of the controlled potential, where a pronounced potential distribution is detected along the electrode. Thus, the potential in the segment near the spigot is always higher than the controlled value and taking into account Fig. 3 it can be concluded that limiting current conditions are not achieved in the last region of the conical part, corroborating that this section of the hydrocyclone is unimportant from an electrochemical standpoint. Likewise, the potential at the top is always more negative than the controlled value giving the possibility of hydrogen evolution in this region despite the controlled potential is in the range of limiting current condition. Fig. 7 also shows a close agreement between the experimental and calculated cathodic potentials near the top. However, a discrepancy is detected for both data sets at the spigot attributable to the uncertainties of the kinetic expression at potentials close to the equilibrium value. The high negative potential at the top region can be

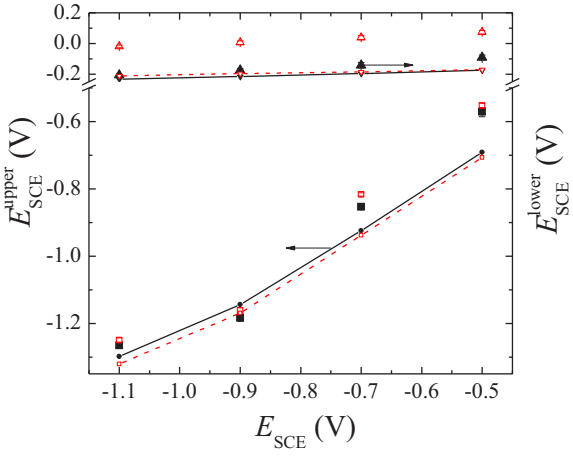

Figure 7. Potentials at the top part, E_{SCE}^{upper}, and at the spigot, E_{SCE}^{lower}, of the hydrocyclone as a function of the controlled cathodic potential. Full symbols: experimental points at $Q = 5.2$ dm^3/min. Open symbols: experimental points at $Q = 8.7$ dm^3/min. Error bars: 95% confidence interval. Full black lines: according to simulations at $Q = 5.2$ dm^3/min. Dashed red lines: according to simulations at $Q = 8.7$ dm^3/min.

explained taking into account Fig. 8, where the θ averaged current distribution at the counter electrode is displayed. Therefore, Fig. 8 shows that the counter electrode presents high current densities in his bottom and low values near the top. This behavior is a consequence of the primary potential distribution of this equipment. The small increase in the current density at $y = 0$ can be attributed to a perturbation of the hydrodynamic conditions due to the inlet port. The overall voltage balance at the axial position y may be written as

$$U = E_a(y) - E_c(y) + \Delta\phi(y) \qquad [35]$$

being E_a the anodic potential, E_c the cathodic one and the last term on the right-hand side represents the ohmic drop in the fluid phase between both electrodes. The three terms on the right-hand side in Eq. 35 depends on the axial position y but its sum is a constant, U, the cell potential difference. Hence, according to Fig. 8 in the region near the top the current density at the counter electrode is lower than that in the controlled potential region, giving lower values of both $E_a(0)$ and $\Delta\phi(0)$. In order to maintain the constant value of U, $E_c(0)$ must take more negative values generating a high current density at the cathode in this region with the possibility of hydrogen evolution as secondary reaction. The above discussion evidences that the current distribution

Table V. Percentage of the total current drained by the secondary reaction.

Q (l/min)	5.2		8.7	
E_{SCE} (V)	Cathode	Anode	Cathode	Anode
–0.5	0	3.8	0	3.32
–0.7	0	22.3	0.1	23.6
–0.9	3.5	31.0	2.8	32.8
–1.1	17.5	44.1	17.6	46.2

in the cylindrical part of the hydrocyclone is strongly influenced by the current distribution at the counter electrode. This fact suggests its consideration in the design of the equipment. The inset in Fig. 8 shows the percentage of the current density at the counter electrode used for ferrocyanide oxidation, reduced species, being the remaining fraction associated to oxygen evolution as secondary anodic reaction. It can be observed that oxygen evolution takes place in all cases in a portion of the counter electrode as a consequence of its high potential distribution and also due to the small range of potential where ferrocyanide oxidation occurs under limiting current conditions, as it is shown in Part (b) of Fig. 3. Depending on the controlled potential value, this behavior is more relevant as the volumetric flow rate is increased, as it is corroborated by Table V.

The comparison of the simulated and experimental values for the cell potential difference and current is displayed in Fig. 9 showing a good agreement between both data sets, which again confirms the validity of the theoretical model.

Uniform current density distribution assumption at the counter electrode.—In order to test both the boundary condition at the counter electrode and the behavior of the model in other reactor configuration, it was considered a simplified 2D electrochemical reactor with parallel-plate electrodes partially facing each other, as it is depicted in the inset of Fig. 10.

Two simulations were performed and are shown in Fig. 10, in the first calculations the kinetic parameters of Table IV were used for the cathode (lower electrode) and for the anode (upper electrode), blue lines, and in the second ones the current density distribution at the anode was imposed uniform by using Eq. 36, red lines.

$$\nabla\phi|_a = \frac{1}{\kappa A_c}\int_{A_c} j dA \qquad [36]$$

A fixed current was imposed, galvanostatic mode, 0.1 A for the full lines and 1 A for the dashed lines. Thus, for the low current sim-

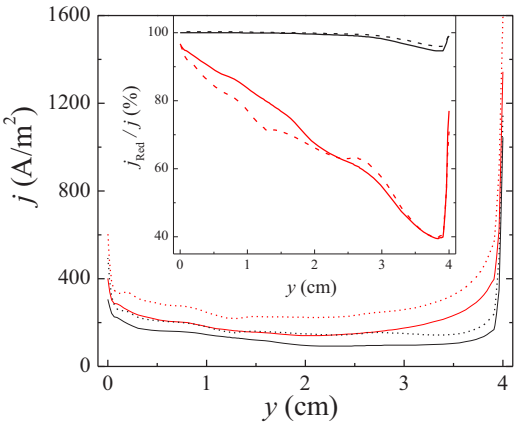

Figure 8. Current distribution at the counter electrode. Inset: fraction of the current density used for ferrocyanide oxidation. Full lines: $Q = 5.2$ dm^3/min. Dashed lines: $Q = 8.7$ dm^3/min. Black lines: $E_{SCE} = -0.5$ V. Red lines: $E_{SCE} = -1.1$ V.

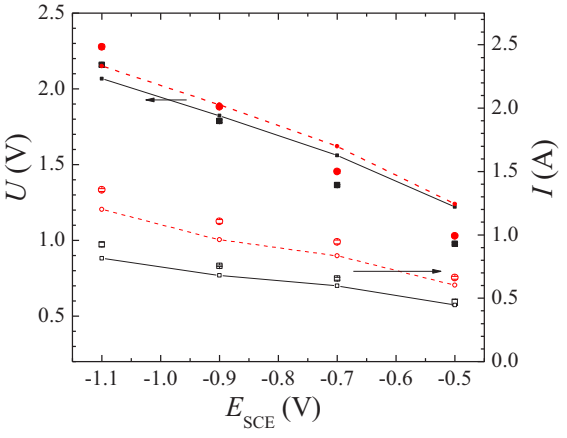

Figure 9. Comparison of the theoretical and experimental values of the cell potential difference and current. Full symbols: U. Open symbols: I. Error bars: 95% confidence interval. Full black lines: according to simulations at $Q = 5.2$ dm^3/min. Dashed red lines: according to simulations at $Q = 8.7$ dm^3/min.

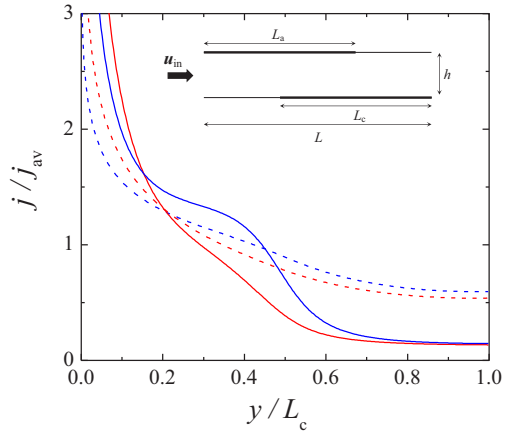

Figure 10. Comparison of theoretical current distributions at the working electrode (cathode) given by the present model, blue lines, with a model assuming a uniform current distribution at the counter electrode, red lines. Full lines: $I = 0.1$ A. Dashed lines: $I = 1$ A. $\boldsymbol{u}_{in} = 0.5$ m/s. $A_a = A_c = 0.01$ m^2, $h = 10$ mm, $L = 0.15$ m, $L_a = L_c = 0.1$ m, $Sc_T = 0.5$.[8] Physicochemical properties and kinetic parameters according to Tables III and IV. Inset: scheme of an electrochemical reactor with parallel-plate electrodes partially facing each other.

ulations the ferricyanide reduction takes place as only reaction at the cathode and for the high current value the secondary reaction becomes predominant. In this way, two different kinetic controls are analyzed.

From Fig. 10 it can be seen that the boundary condition at the counter electrode has an important influence on the current distribution at the working electrode, even at low currents, being more marked for the case of uniform current distribution at the counter electrode. This fact can be explained taking into account Eq. 35, which reveals that a low value in E_a imposes a more negative cathodic potential in order to maintain U constant along the axial direction. Finally, the calculated cell potential differences in this last case were 23% and 29% higher than the values given by the actual model for I 0.1 A and 1 A, respectively.

Conclusions

A mathematical model to calculate the tertiary current distribution based on the simultaneous solution of the hydrodynamics, k averaged convection-diffusion equations and Laplace's equation resulted suitable to predict experimental results obtained with a modified hydrocyclone as electrochemical reactor. The model considers multiple reactions at each electrode with different kinetic controls.

The tertiary current distribution model was solved by means of a computational algorithm based on a control-volume formulation which was implemented in OpenFOAM as a free source compact and general tool. It has a native 3D support and is suitable of execution in parallel computers, showing a fast convergence and good accuracy. The solver is given as a GitHub link[27] for the reader to use or modify it.

The experimental and theoretical results corroborated that the modified hydrocyclone presents a marked current distribution in axial direction being the performance of the cylindrical part better than the conical one from an electrochemical standpoint.

Theoretical analysis confirmed that it is extremely important to know the kinetic behavior of all reactions involved at the counter electrode as well as at the working electrode, in order to accurately predict the current and potential distribution in the whole reactor. Imposing a constant current density at the counter electrode can give important errors.

The present formulation allows to the user to verify, previous to experimental measurement of mass-transfer coefficients, if any of the electrodes have any risk to have secondary reactions.

A modified hydrocyclone can be considered as a promising reactor to carry out electrochemical reactions under mass-transfer control with the generation of a solid reaction product. Examples of these types of electrochemical systems are the recovery of metals from effluents or the production of colloidal sulfur by means of the reduction or oxidation of sulfur compounds. In these cases the good mass-transfer conditions of the cylindrical part of the hydrocyclone allow a high efficiency and the solid product is detached from the electrode surface by the impingement of the liquid phase, being the largest particles separated through the spigot of the equipment.

Acknowledgments

This work was supported by Agencia Nacional de Promoción Científica y Tecnológica (ANPCyT), Consejo Nacional de Investigaciones Científicas y Técnicas (CONICET) and Universidad Nacional del Litoral (UNL) of Argentina.

List of Symbols

A	parameter given by Eq. 16
A	electrode surface area (m^2)
a_k	parameter given by Eq. 14
B	parameter given by Eq. 17
b_k	parameter given by Eq. 15
b_T	Tafel slope $= RT/\alpha F$ or $-RT/(1-\alpha)F$ (V)
c	local concentration or time-averaged concentration (mol/m^3)
D	diffusion coefficient (m^2/s)
D_T	turbulent diffusion coefficient (m^2/s)
d_h	hydraulic diameter (m)
diffRef	expression given by Eq. 31 or by Eq. 32
E	electrode potential (V)
E_0	reversible electrode potential (V)
f	function defined in Eqs. 18, 20 and 23
F	Faraday constant = 96485 (C/mol)
h	inter-electrode gap (m)
I	current (A)
j	current density (A/m^2)
j_0	exchange current density (A/m^2)
k	turbulence kinetic energy (m^2/s^2)
L	electrode length (m)
maxRef	input supplied by the user
max$U$	maximum cell potential expected for the simulation
n	coordinate normal to surface (m)
p	density normalized pressure (m^2/s^2)
Q	volumetric flow rate (m^3/s or l/min)
r	radial coordinate (m)
R	universal gas constant = 8.314 (m^{3}Pa/K/mol)
Res	residual value
Sc_T	turbulent Schmidt number $= \nu_T/D_T$
t	time (s)
T	temperature (°C or K)
TI	turbulence intensity
Tol	tolerance value
$\boldsymbol{u}$	fluid velocity (m/s)
U	cell potential difference (V)
var	ϕ or c_k
VR	function defined in Eqs. 18, 21 and 24
VGR	function defined in Eqs. 18, 19 and 22
y	axial coordinate (m)

Greek

α	charge transfer coefficient
β	under-over relaxation parameter used in Eq. 33
Δ	distance between the cell center to the interface
η	overvoltage (V)

θ	angular coordinate (rad)
κ	fluid phase conductivity (S/m)
ν	kinematic viscosity (m^2/s)
ν_e	charge number of the electrode reaction
ν_k	stoichiometric coefficient of the k^{th} species
ν_T	turbulent kinematic viscosity (m^2/s)
ϕ	potential (V)
ω	turbulence frequency or specific dissipation rate (1/s)

Others Characters

Δ	Delta operator
∇	Nabla operator
∂	partial derivative

Subscripts and Superscripts

a	anodic
av	average
b	bulk
c	cathodic
center	referred to cell or volume element center
c_k	referred to the concentration of the k^{th} species
face	referred to cell or volume element face
i	referred to the i^{th} reaction
in	inlet
k	referred to the k^{th} species
$\neq$k	product of the reaction which reactant is k
lim	limiting value
lower	measured potential at the spigot
out	outlet
ref	reference
ref_d	desired reference
s	solid phase
SCE	saturated calomel electrode
T	transpose of a tensor
upper	measured potential at the top
w	wall
ϕ	referred to the potential
0	older iteration step
*	intermediate iteration step

ORCID

A. N. Colli https://orcid.org/0000-0002-0983-1842

J. M. Bisang https://orcid.org/0000-0001-9120-7418

References

1. D. J. Pickett, *Electrochemical Reactor Design*, Elsevier, Amsterdam (1979).
2. J. Newman and K. E. Thomas-Alyea, *Electrochemical Systems, 3rd ed*, Wiley-Interscience (2004).
3. J. Deconinck, *Current distributions and electrode shape changes in electrochemical systems*, Springer Science & Business Media (2012).
4. A. N. Colli and H. H. Girault, *J. Electrochem. Soc.*, **164**, E3465 (2017).
5. A. N. Colli and J. M. Bisang, *Electrochim. Acta*, **290**, 676 (2018).
6. A. N. Colli and J. M. Bisang, *J. Electrochem. Soc.*, **160**, E5 (2013).
7. A. N. Colli and J. M. Bisang, *J. Electrochem. Soc.*, **164**, E42 (2017).
8. A. N. Colli and J. M. Bisang, *J. Electrochem. Soc.*, **165**, E81 (2018).
9. L. F. Catañeda, F. F. Rivera, T. Pérez, and J. L. Nava, *Curr. Opin. Electrochem.*, **16**, 75 (2019).
10. P. Byrne, P. Bosander, O. Parhammar, and E. Fontes, *J. Appl. Electrochem.*, **30**, 1361 (2000).
11. F. F. Rivera, P. E. Hidalgo, F. Castañeda-Záldivar, I. R. Terol-Villalobos, and G. Orozco, *Chem. Eng. J.*, **355**, 457 (2019).
12. V. Boovaragavan and C. A. Basha, *J. Appl. Electrochem.*, **36**, 745 (2006).
13. C. T. J. Low, E. P. L. Roberts, and F. C. Walsh, *Electrochim. Acta*, **52**, 3831 (2007).
14. T. Pérez and J. L. Nava, *J. Electroanal. Chem.*, **719**, 106 (2014).
15. M. Rosales and J. L. Nava, *J. Electrochem. Soc.*, **164**, E3345 (2017).
16. J. D. Yang and A. C. West, *AIChE J.*, **43**, 811 (1997).
17. E. P. Rivero, M. R. Cruz-Díaz, F. J. Almazán-Ruiz, and I. González, *Chem. Eng. Res. Des.*, **100**, 422 (2015).
18. M.-H. Chung, *Electrochim. Acta*, **45**, 3959 (2000).
19. J. N. Harb and R. C. Alkire, *J. Electrochem. Soc.*, **138**, 3568 (1991).
20. P. Byrne, E. Fontes, O. Parhammar, and G. Lindbergh, *J. Electrochem. Soc.*, **148**, D125 (2001).
21. N. Weber, S. Landgraf, K. Mushtaq, M. Nimtz, P. Personnettaz, T. Weier, J. Zhao, and D. Sadoway, *Electrochim. Acta*, **318**, 857 (2019).
22. A. N. Colli and J. M. Bisang, *Electrochim. Acta*, **137**, 758 (2014).
23. L. C. Resio, O. González Pérez, and J. M. Bisang, *J. Electrochem. Soc.*, **164**, E529 (2017).
24. A. N. Colli, J. P. Fornés, O. González Pérez, and J. M. Bisang, *Electrochim. Acta*, **309**, 219 (2019).
25. F. Moukalled, L. Mangani, and M. Darwish, *The Finite Volume, Method in Computational Fluid Dynamics: An Advanced Introduction with OpenFOAM and Matlab*, Springer International Publishing (2015).
26. A. N. Colli and J. M. Bisang, *Int. J. Heat Mass Transfer*, **137**, 835 (2019).
27. A. N. Colli, (2019), https://github.com/ancolli/tertiaryCurrentDistributionFoam.
28. D. Bradley, *The Hydrocyclone*, Pergamon Press, Oxford (1965).
29. R. Battino, T. R. Rettich, and T. Tominaga, *J. Phys. Chem. Ref. Data*, **12**, 163 (1983).
30. R. C. Weast and M. J. Astle, *Handbook of Chemistry and Physics, 62 Edition, CRC press*, Inc., Boca Raton, Florida. USA (1981).
31. C. Aldrich, in *Progress in Filtration and Separation*, S. Tarleton Editor, p. 1, Academic Press, Oxford (2015).
32. P. Dinesh Suresh, V. Kumar, R. Sripriya, S. Chakraborty, and B. C. Meikap, *Chem. Eng. Sci.*, **65**, 4661 (2010).
33. Y. R. Murthy and K. U. Bhaskar, *Powder Technol.*, **230**, 36 (2012).
34. C. Banerjee, K. Chaudhury, A. K. Majumder, and S. Chakraborty, *Ind. Eng. Chem. Res.*, **54**, 522 (2015).